Behaviour of elevated concrete silos filled with saturated solids

Mohamed T. Abdel-Fattah, Ian D. Moore, and Tarek T. Abdel-Fattah

Abstract: A finite-element solution is introduced for simulating the filling process of elevated concrete silos filled with saturated solids. An axisymmetric finite-element model is used to represent both the solids and the structure. The bulk solids are modeled using an elastoplastic model, whereas the structure is modeled using a linear elastic model. The interaction between the two materials is modeled using interface elements to permit relative movement. The filling process is idealized via a multistage numerical technique capable of representing both undrained and drained conditions. The effect of the filling process may be time-dependent. The excess pore-water pressure caused by the filling process may significantly influence the magnitudes of internal forces. Moreover, the design critical sections of the same silo element may correspond to different bulk solid conditions (undrained or drained). Practically, the ring beam stiffness may only influence hoop compressions in the silo elements at the wall–hopper junction. The results presented may be used to design tests to evaluate existing silos.

Key words: elevated concrete silos, silo filling, finite-element analysis, elastoplastic model, consolidation, hopper, ring beam stiffness.

Résumé : Une solution par éléments finis pour la simulation du processus d'ensilage des silos en béton surélevés remplis de solides saturés est présentée. Un modèle par éléments finis axisymétriques est utilisé pour représenter à la fois les solides et la structure. Les solides en vrac sont modélisés en utilisant un modèle élasticimétrique, alors que la structure est modélisée en utilisant un modèle élastique linéaire. L'interaction entre les deux matériaux est modélisée en utilisant des éléments d'interface afin de permettre un mouvement relatif. Le processus de remplissage est idéalisé par une technique numérique à plusieurs étages capable de représenter à la fois les conditions non drainées et les conditions drainées. L'effet du processus d'ensilage peut être dépendant du temps. La pression interstitielle excessive causée par le processus d'ensilage peut grandement influencer les amplitudes des forces internes. De plus, les sections importantes pour la conception du même élément de silo peuvent correspondre à différentes conditions de solides en vrac (non drainés et drainés). En pratique, la rigidité de la poutre annulaire peut seulement influencer les compressions des cerceaux dans les éléments de silos à la jonction mur-trémie. Les résultats présentés peuvent être utilisés pour concevoir des essais visant à évaluer les silos existants.

Mots clés : silo en béton surélevé, ensilage, analyse par éléments finis, modèle élasticimétrique, consolidation, trémie, rigidité de la poutre annulaire.

[Traduit par la Rédaction]

Introduction

The static pressure induced by a stored material on a silo wall is a significant component of the critical load combination, which may also include dynamic forces because of

M.T. Abdel-Fattah. Construction Research Institute, National Water Research Centre, Kanater, Cairo 13621, Egypt.
I.D. Moore.[1] GeoEngineering Centre at Queen's – Royal Military College of Canada (RMC), Department of Civil Engineering, Ellis Hall, Queen's University, Kingston, ON K7L 3N6, Canada.
T.T. Abdel-Fattah. Housing and Building Research Centre, Cairo 11511, Egypt.

[1]Corresponding author (e-mail: moore@civil.queensu.ca).

loading or unloading, thermal effects, and seismic or wind loads. Hatfield and Bartali (1988) reported that the dynamic effect may be incorporated in the loading combination by multiplying the static pressure by an amplification factor, a practice adopted by a number of silo design standards (e.g., American Concrete Institute standard 313-97 (ACI 1997), and Deutsches Institut für Normung standard 1055 (DIN 1987)). The present study focuses on the static loading on the silo elements (wall, hopper, ring beam, and supporting wall) due to the filling process.

Silo walls are primarily subjected to hoop (circumferential) tension due to the pressure exerted by the solids on the wall and axial (meridianal) compression due to the friction mobilized at the interface, in addition to the wall self-weight. Hoop compression may also develop in the vicinity of the wall–hopper junction with magnitudes that are dependent on the stiffnesses of the silo elements at that location. They may also be subjected to meridianal and circumferential bending moments and radial shear forces. This is dependent on the pressure pattern (symmetric or

nonsymmetric) to which the wall is subjected and (or) the wall boundary conditions. Two general approaches for the analysis and design of silo walls may be followed (Abdel-Sayed et al. 1985). In the first approach the pressure induced by the bulk solids on the wall is established with no account for the interaction between the two materials, whereas in the second approach the composite system of the ensiled material and wall is regarded as a continuum discretized by a number of finite elements (e.g., Bishara et al. 1977; Ooi and Rotter 1990). The first approach is adopted by most silo design codes where the lateral pressures on the wall are established using either of the two classic silo theories, namely Janssen's theory (Janssen 1895) and the Reimbert theory (Reimbert and Reimbert 1976), as alternatives to the determination of the theoretical pressures. The two theories differ fundamentally in the assumption adopted for calculating the pressure ratio (ratio of horizontal to vertical pressures), where this ratio is assumed to be constant in Janssen's theory but to decrease with depth in the Reimbert theory. Yet, the pressure ratio and the bulk solids unit weight are assumed to increase with an increase in depth in the specialized version of Janssen's theory (Cowin 1979). Briassoulis (1991) reported that the Reimbert theory overestimates the lateral pressures compared with Janssen's theory and that a number of investigators (e.g., Bishara et al. 1983; Abdel-Sayed et al. 1985) consider Janssen's theory as being inaccurate and unconservative.

Janssen's (1895) silo theory has constituted the basis of silo design for many decades. This theory accounts for the arching effect within the bulk solids and allows for transfer of part of their weight to the wall in shear where it is carried to the base of the silo as wall thrust. It suggests that the horizontal pressure P may be established as

$$[1] \qquad P = \frac{\gamma_s r [1 - \exp(-2K\mu_s y/r)]}{2\mu_s}$$

in which γ_s is the average unit weight of stored material; r is the silo radius; y is the depth measured from the top of the silage; μ_s is the coefficient of friction between the stored material and the wall; and K is the ratio of mean horizontal to mean vertical pressures, assumed equal to the Rankine's coefficient of static earth pressure (e.g., Gurfinkel 1979; Gaylord and Gaylord 1984):

$$[2] \qquad K = (1 - \sin\varphi)/(1 + \sin\varphi)$$

where φ is the angle of internal friction. Experimental studies on deep silos carried out by Pieper and Wenzel (1964) revealed that Janssen's silo theory could lead to better results by calculating the coefficient K as

$$[3] \qquad K = 1 - \sin\varphi$$

equivalent to the coefficient for the "at-rest" (zero lateral strain) condition. This naturally leads to higher pressures on the silo wall. Furthermore, Briassoulis (1991) reported that many investigators (e.g., Cowin 1979; Dabrowski 1985) had shown analytically that K may be bounded by

$$[4] \qquad (1 - \sin\varphi)/(1 + \sin\varphi) < K < 1$$

and therefore eq. [2] merely represents a lower bound for the pressure ratio K.

As a step towards defining more realistic rigorously based pressure distributions on silo walls, Ooi et al. (1990) measured both the filling and discharge pressures on a prototype tall concrete silo storing barley. The statistical analyses of the eight experiments conducted in the same prototype silo showed that the design storing pressures may be 50% higher than the Janssen values based on the experimental best-fit bulk solid properties. It was also concluded that most silo codes tend to consistently overestimate the wall friction coefficient (an unconservative practice) and may partly compensate by overestimating the lateral pressure ratio (a conservative practice).

Because of the potential development of nonsymmetrical pressures due to the stored material, a free (patch) load acting on any part of the silo wall may be considered. This approach has been adopted by a number of codes of practice (e.g., Deutsches Institut für Normung standard 1055 (DIN 1987), and European Committee for Standardization Eurocode EN 1991-4 (ECS 2004)). These nonsymmetrical pressures may be unavoidable even in axisymmetric silos with concentric filling, since they may arise as a result of geometric imperfections in the wall and probabilistic changes in the bulk solid properties (Briassoulis 1998). The results from the experiments conducted by Ooi et al. (1990) revealed that quite large systematic nonsymmetrical pressures occur during filling and storing, as well as during discharge. Using the nonsymmetric pressure distributions measured by Ooi et al., Briassoulis (1998) conducted a finite-element analysis for the shell structure to establish the state of stress in the shell and concluded that the design of silo walls might not neglect the asymmetric features of the real pressures developed by the stored material. The effect of the nonsymmetric pressure is not considered here, however, because it is out of the scope of this investigation.

Conical discharge hoppers are normally subjected to symmetrical loading from the stored material. The most commonly used theories for pressures in hoppers are those of Walker (1966), Walters (1973), and Jenike et al. (1973). Rotter (1990) reported that most codes of practice specify either a constant pressure within the hopper or a linearly varying pressure, in addition to a local "switch" pressure near the wall–hopper junction to account for flow conditions. Naturally, the vertical load on the hopper is maximized when the pressure on the wall is minimized. This condition is met when both K and μ_s in eq. [1] take their minimum values. Equation [2] may be used to obtain a minimum value for K. Alternatively, Rotter (1990) showed that a more realistic value of K can be derived from the relation first introduced by Walker (1966) as

$$[5] \qquad K = \frac{1 + \sin^2\varphi - 2\sqrt{\sin^2\varphi - \mu_s^2 \cos^2\varphi}}{4\mu_s^2 + \cos^2\varphi}$$

The values of K estimated from eqs. [2] and [5] differ only slightly unless the wall is considerably rough (Rotter 1990).

Another aspect of silo design also requires consideration, namely the behaviour of wet silage and the potential effects of consolidation during or after the filling process. Design standards like the *National Farm Building Code of Canada* (NRCC 1995) require any zone of saturated silage to be identified and silo wall pressures to include explicit consid-

eration of hydrostatic pressures acting against the wall in the zone of saturated material at the base of the silo. This generally makes a very substantial contribution to the lateral wall pressures and can lead to much greater wall strength requirements. Design of "class II" structures (those expected to hold wet silage) requires assessment of lateral pressures associated with high filling speed, neglecting any influence of "primary consolidation" of the ensiled material (reductions in pore-water pressure, as water drainage leads to compression of that material). Consolidation may actually occur, so lateral pressures and consequently the design requirements of the silo elements may depend on the speed with which the silo can be filled (Abdel-Fattah et al. 2005).

An understanding of the loading speed and the effect of silage consolidation is investigated in this paper, using numerical simulations of the filling process to estimate the forces that develop in an elevated concrete silo filled with saturated sand. Calculations are performed assuming that the filling process is completed over a predefined number of stages, with consolidation allowed following completion of each stage. Accordingly, the number and frequency of (time elapsed between) the filling stages are expected to affect the patterns of forces developed in the structure, given the reoccurring pattern of development and dissipation of the excess pore pressure within the bulk solids. For consolidating silage, the structure must be designed to withstand the temporary forces developed due to the undrained conditions, where out-of-equilibrium water pressures may exceed those due to silage in a drained (consolidated) condition.

One particular silo geometry (Fig. 1) is used here to examine the effects of silage consolidation on the internal forces that develop in the structure due to filling. Also, the pressure patterns on the silo wall and hopper are established taking into account the state of the bulk solids (undrained or drained) during the filling process. The effects of the ring beam stiffness and wall top boundary conditions on the internal forces in the silo elements are also examined.

Geometric and material properties

Figure 1 displays the geometric properties of the example silo and the definitions of its different elements. It is assumed that the silo is supported by a continuous wall built in at its bottom. The discharge-opening lid has a thickness of 0.40 m and is modeled as a circular plate pinned to the opening perimeter. The silo wall thickness varies from 0.30 m at the wall–hopper junction to 0.15 m over a height of 3.0 m, beyond which the wall thickness remains constant. The silo geometry proposed here is not intended as an adequate design. The total height of silage (13.50 m) is divided into 13 layers each of 1.0 m thickness and a bottom layer of 0.50 m thickness.

Six filling schemes are examined as follows: (1) one layer of thickness 13.50 m; (2) two layers of thicknesses 8.50 and 5.00 m; (3) three layers of thicknesses 4.50, 5.00, and 4.00 m; (4) four layers of thicknesses 4.50 m for the first layer and 3.00 m for each subsequent layer; (5) six layers of thicknesses 3.50 m for the first layer and 2.00 m for each subsequent layer; and (6) 11 layers of thicknesses 2.50 m for the first layer, 2.00 m for the second layer, and 1.00 m for each subsequent layer.

Concrete is modeled as a linear elastic material with Young's modulus $E = 25.0$ GPa and Poisson's ratio $\nu = 0.20$. The design of the silo element cross sections is based on a concrete characteristic cube strength of 30 MPa and steel yield stress of 360 MPa.

For the ensiled material (saturated sand), the material-hardening constitutive model (Schanz 1998) adopted by the finite-element code PLAXIS (Brinkgreve and Vermeer 1998) is used. This model is used for simulating the behaviour of both soft and stiff soils. It has a yield surface that is not fixed in the principal stress space. Both shear hardening and compression hardening are represented in the model. The basic assumption in the model formulation is that the relationship between the vertical strain ε_1 and the deviatoric stress q in the primary triaxial loading can be approximated by a hyperbola as shown in Fig. 2.

The hyperbolic relationship plotted in Fig. 2 can be described by

$$[6] \qquad -\varepsilon_1 = \frac{1}{2E_{50}} \frac{q}{1 - q/q_a} \qquad \text{for} \qquad q < q_f$$

where E_{50} is a confining-stress-dependent stiffness modulus for primary loading; and q_f and q_a are, respectively, the ultimate and asymptotic deviatoric stresses, which can be obtained from the relations

$$[7] \qquad q_f = (c \cot \varphi - \sigma_3') \frac{2 \sin \varphi}{1 - \sin \varphi}$$

and

$$[8] \qquad q_a = q_f / R_f$$

where c is the cohesion, φ is the angle of internal friction, σ_3' is the confining pressure in a triaxial test, and R_f is a failure ratio that should be smaller than unity. The stiffness modulus E_{50} is given by

$$[9] \qquad E_{50} = E_{50}^{\text{ref}} \left(\frac{c \cot \varphi - \sigma_3'}{c \cot \varphi + P^{\text{ref}}} \right)^m$$

where E_{50}^{ref} is a reference stiffness modulus corresponding to the reference confining pressure P^{ref}, and m is the power of stress-level dependency of stiffness that is normally assumed to have values around 0.50 for sands and silts as reported by Janbu (1963).

For unloading and reloading stress paths, the model uses another stress-dependent stiffness modulus defined by

$$[10] \qquad E_{ur} = E_{ur}^{\text{ref}} \left(\frac{c \cot \varphi - \sigma_3'}{c \cot \varphi + P^{\text{ref}}} \right)^m$$

where E_{ur}^{ref} is the reference stiffness modulus for unloading and reloading corresponding to the reference confining pressure P^{ref}, normally taken equal to $3E_{50}^{\text{ref}}$ in many practical situations as cited in the PLAXIS user's manual (Brinkgreve and Vermeer 1998). The oedometer stiffness E_{oed} for one-dimensional compression is defined by

$$[11] \qquad E_{oed} = E_{oed}^{\text{ref}} \left(\frac{c \cot \varphi - \sigma_1'}{c \cot \varphi + P^{\text{ref}}} \right)^m$$

Fig. 1. Geometric properties of the example silo and definitions of its different elements.
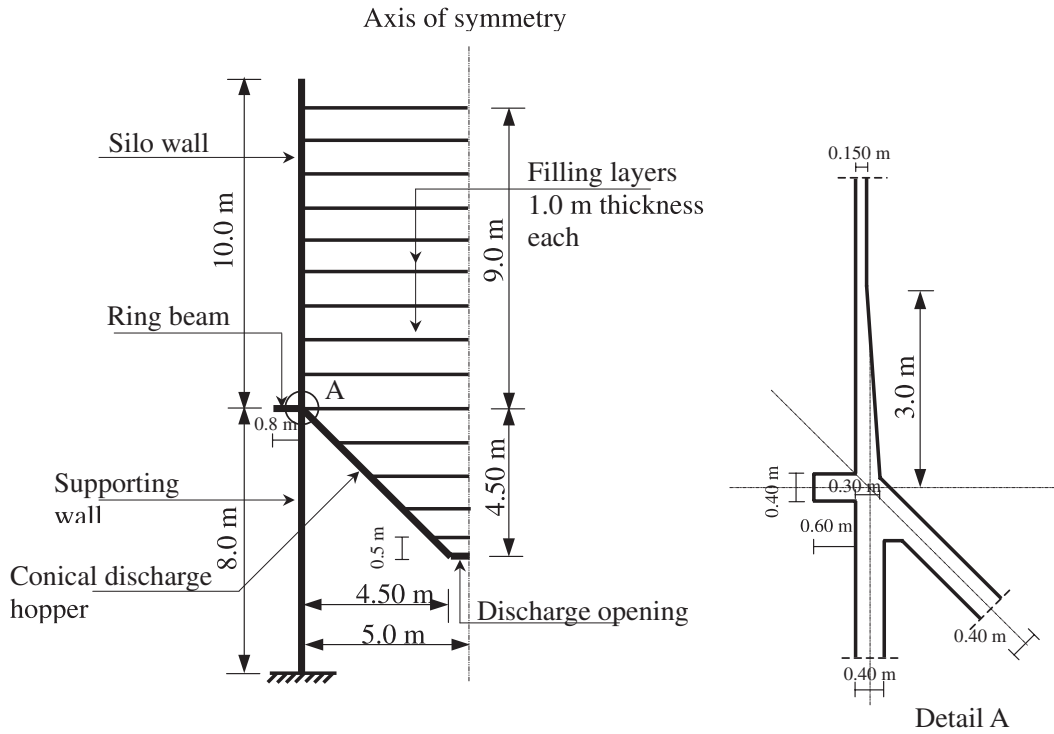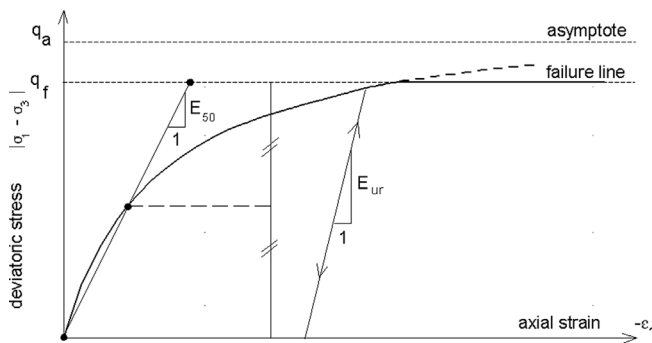

Fig. 2. Hyperbolic stress–strain relationship in primary loading for a standard drained triaxial test. Adapted from the PLAXIS user's manual (Brinkgreve and Vermeer 1998).

where E_{oed}^{ref} is a tangent stiffness at a vertical stress of $-\sigma_1' = P^{ref}$. The model's yield function is defined by

[12] $\quad f = \bar{f} - \gamma^p$

where $\bar{f}$ is a function of stress given by

[13] $\quad \bar{f} = \dfrac{1}{E_{50}} \dfrac{q}{1 - q/q_a} - \dfrac{2q}{E_{ur}}$

and γ^p is a function of plastic strains defined by

[14] $\quad \gamma^p = -(2\varepsilon_1^p - \varepsilon_v^p) \approx -2\varepsilon_1^p$

in which ε_1^p and ε_v^p are, respectively, the axial and volumetric plastic strains.

For primary loading where $\gamma^p = \bar{f}$,

[15] $\quad -\varepsilon_1^p \approx \dfrac{1}{2}\bar{f} = \dfrac{1}{2E_{50}} \dfrac{q}{1 - q/q_a} - \dfrac{q}{E_{ur}}$

The elastic strains that develop during primary loading and unloading–reloading are defined by

[16] $\quad -\varepsilon_1^e = q/E_{ur}; \qquad -\varepsilon_2^e = -\varepsilon_3^e = -\nu_{ur} q/E_{ur}$

where ν_{ur} is the unloading–reloading Poisson's ratio.

From eqs. [15] and [16], the axial strain in the deviatoric stage of the triaxial test can be written as

[17] $\quad -\varepsilon_1 = -\varepsilon_1^e - \varepsilon_1^p \approx \dfrac{1}{2E_{50}} \dfrac{q}{1 - q/q_a}$

The relation between the rates of plastic shear strain and plastic volumetric strain (indicated by the overdots) is governed by the flow rule

[18] $\quad \dot{\varepsilon}_v^p = \sin\psi_m \dot{\gamma}^p$

where ψ_m is the mobilized angle of dilatancy defined by

[19] $\quad \sin\psi_m = \dfrac{\sin\varphi_m - \sin\varphi_{cv}}{1 - \sin\varphi_m \sin\varphi_{cv}}$

in which φ_{cv} is the critical state friction angle; and φ_m is the mobilized friction angle, defined by

[20] $\quad \sin\varphi_m = \dfrac{\sigma_1' - \sigma_3'}{\sigma_1' + \sigma_3' - 2c\cot\varphi}$

The critical state friction angle can be obtained by replacing the mobilized friction and dilatancy angles in eq. [19] by their values at failure (φ and ψ), and hence

[21] $\quad \sin\varphi_{cv} = \dfrac{\sin\varphi - \sin\psi}{1 - \sin\varphi\sin\psi}$

The present study is carried out assuming that the example silo is filled with saturated sand, a material used previously by many investigators (e.g., Briassoulis 1991; Holst et al. 1999) in silo loading studies. The material parameters assigned to the saturated sand are assumed to be as follows: $E_{50}^{ref} = 1.20 \times 10^5$ kN/m^2, $E_{oed}^{ref} = 1.33 \times 10^5$ kN/m^2, $E_{ur}^{ref} = 3.60 \times 10^5$ kN/m^2, $\nu_{ur} = 0.20$, $P^{ref} = 200$ kN/m^2, $\varphi = 33°$, $\psi = 3°$, $m = 0.50$, dry unit weight $\gamma_d = 17$ kN/m^3, wet unit weight $\gamma_{wt} = 21$ kN/m^3, coefficient of isotropic permeability = 0.50 m/day, and $c^{ref} = 10.0$ kN/m^2.

Finite-element model

Description of the model and procedure

An axisymmetric finite-element model is used to represent the concrete silo and the saturated sand. The silo structure is modeled using three-noded beam elements, whereas the solids are modeled using six-noded triangular solid elements. Although "beams" are actually one-dimensional structures, beams in PLAXIS represent real plates in the out-of-plane direction and can therefore be used to model walls and plates. A typical finite-element mesh is shown in Fig. 3. The model is restrained in the radial direction at the axis of symmetry. The wall is restrained in the radial direction at its top. A closed consolidation boundary is imposed along the axis of symmetry, since no flow is permitted through this boundary.

The interaction between the silo wall and bulk solids is modeled using interface elements. The use of these elements permits modeling of an interface condition between the smooth (no friction) and rough (full compatibility) limits. A strength factor R_{int} is introduced to define the strength parameters of the interface (subscript "int") relative to those of the original material (subscript "s"), thus

[22a] $\quad c_{int} = R_{int}c_s$

[22b] $\quad \tan\varphi_{int} = R_{int}\tan\varphi_s$

[22c] $\quad G_{int} = R_{int}^2 G_s \leq G_s$

and

[22d] $\quad E_{oed,int} = 2G_{int}(1 - \nu_{int})/(1 - 2\nu_{int})$

with a default value of 0.45 for the interface material Poisson's ratio ν_{int}.

Throughout this investigation, a value of 0.70 is assigned to the strength factor R_{int}, a typical value for the strength parameter of a sand–concrete interface.

The interface element has a virtual thickness, but in the finite-element formulation the coordinates of the reciprocal nodes are coincident. The virtual thickness may be established by multiplying the average element size by a virtual thickness factor.

Abdel-Fattah et al. (2005) conducted a finite-element analysis on a ground-supported concrete silo to examine the sensitivity of the results obtained to the virtual thickness assumed and suggested that a value of 0.10 assigned to this factor may be appropriate for the purpose of their numerical investigation, which concerns a structure with specific geo-

Fig. 3. A typical finite-element mesh.
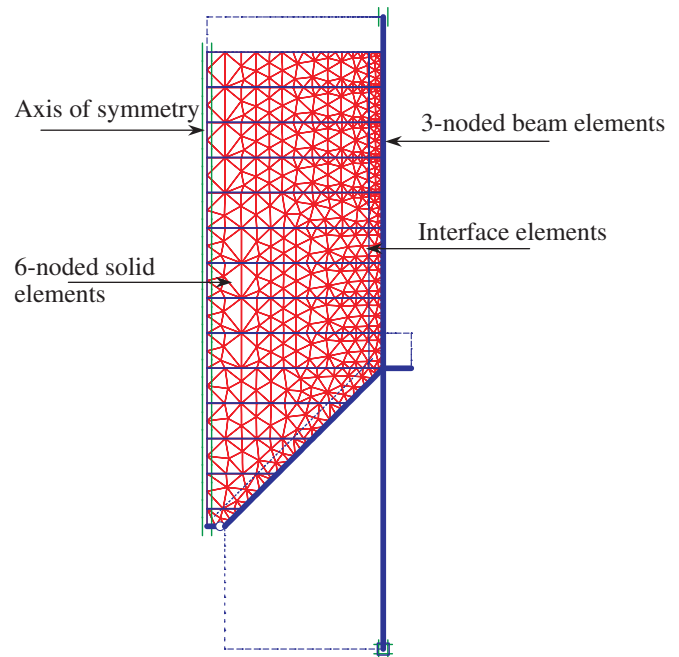
metric and material properties. Therefore, throughout this investigation, a default value of 0.10 is assigned to this factor, since no measurements are available at this stage of the investigation.

The filling process is simulated in the finite-element model via a multistep analysis strategy, with the ensiled material placed in a number of layers of an arbitrary thickness. For each layer, an undrained analysis is first performed to estimate the excess pore-water pressures in the bulk solids, followed by a drained analysis to allow these pressures to fully dissipate prior to adding the subsequent layer.

Comparison with a closed-form solution

Hatfield and Bartali (1988) introduced a closed-form solution for the static forces and moments in a grain silo. The proposed silo material is homogenous, isotropic, and linearly elastic, and the wall thickness is small compared with the radius. The silo is full of grain but not heaped. Horizontal grain pressure, P, is given by Janssen's formula (eq. [1]). The aforementioned assumptions result in axially symmetric forces and deformations. These forces are the hoop force N_θ, axial force N_ϕ, radial shear Q_r, and meridianal bending moment M_ϕ.

An example silo, with the properties examined by Hatfield and Bartali (1988), was analyzed using the solution given earlier in the paper: height of 15.0 m, radius of 3.0 m, and wall thickness of 0.155 m. The wall material has a Young's modulus of 25.0 GPa, Poisson's ratio of 0.30, and unit weight of 24 kN/m^3. The grain properties are $\gamma_s = 8.0$ kN/m^3, $K = 0.31$, and $\mu_s = 0.40$. This structure is taller than that examined in the subsequent sections studying silage consolidation, so it is used here to assess whether the finite-element analysis can reproduce the full Janssen arching behaviour. In the finite-element solution, the angle of internal friction and the interface strength factor R_{int} are taken as

equal to 33° and 0.67, respectively; this is to produce the same values considered for the parameters K and μ_s in the closed-form solution. The bottom boundary of the finite-element model is restrained in the vertical direction.

A comparison between the results obtained from both the closed-form solution and the present finite-element solution for the limiting case of zero restraint at the bottom edge of the silo is shown in Fig. 4. Plotted in Fig. 4a are the pressure distributions obtained from the finite-element solution together with those from Janssen's theory using values for K of 0.31 and 0.46, which correspond to the active and at-rest conditions of earth pressure, respectively. From Fig. 4a, it can be seen that for the structure with the geometric properties and boundary conditions proposed here, Janssen's theory using an active earth pressure coefficient underestimates the wall pressure. This becomes more pronounced near the silo base where the finite-element solution predicts a sharp increase in the pressure along the lower fifth of the silo height. At the silo base, an increase in the pressure of 45% is predicted. On the other hand, the wall pressure distribution obtained from the finite-element analysis is in very good agreement with Janssen's predictions using the coefficient of earth pressure at rest except for at the base where Janssen's theory underestimates the pressure by 18%. The same observations may be made from Fig. 4b, which presents the axial and hoop force distributions along the silo height for $K = 0.31$.

The discrepancies between the results obtained from both solutions may be expected, since it was previously shown by many investigators (e.g., Pieper and Wenzel 1964; Cowin 1979; Dabrowski 1985) that better estimations can be obtained from Janssen's theory if values for K higher than that calculated from eq. [1] are used. Another source for these discrepancies could be due to the fact that the solution of Hatfield and Bartali (1988) does not account for the effect of the relative stiffness between the bulk solids and concrete structure. This is not the case with the finite-element solution obtained here where the bulk solid parameters vary along the silo wall according to the level of the confining pressure within the bulk solids.

As shown later in this investigation, however, finite-element predictions have been obtained for the lateral pressures that are in very good agreement with Janssen's predictions using the coefficient of active earth pressure. Those predictions have been obtained using a silo structure with a hopper with aspect ratio of 1.00 relative to 2.50 for the structure analyzed here and with different wall boundary conditions.

Results of analyses and discussion

Variation of the excess pore-water pressure
The variation of the excess pore pressure within the bulk solids with time for a point located in the middle of the bottom layer is plotted in Fig. 5. At time $T = 0.0$ (assuming an instantaneous filling process) in Fig. 5, a maximum excess pore-water pressure of about 200 kN/m^2 is predicted due to filling scheme 1. On the other hand, a minimum excess pore-water pressure of about 36 kN/m^2 is predicted due to filling scheme 6. The estimated time for full dissipation of

the excess pore pressure is about 27 and 80 min for filling schemes 1 and 6, respectively. The former is associated with one period following complete filling, whereas the latter is associated with 11 time intervals following the corresponding filling stages.

Pressures on wall and hopper
Depending on the bulk solids condition (undrained or drained) during filling, two types of pressures on the wall and hopper can be distinguished. The first is due to the excess pore-water pressures that develop within the bulk solids under the undrained condition, whereas the second is due to the resulting effective stresses following dissipation of the excess pore-water pressures (i.e., drained condition) within the bulk solids. Therefore, under the undrained condition, for the current filling stage, the part of the silo element (wall or hopper) loaded in this stage is only subjected to hydrostatic pressure, whereas those parts which were loaded in the preceding filling stages are subjected to pressures from both effective stresses (resulting from the preceding stages) and hydrostatic pressure (resulting from the current filling stage). Under the fully drained condition for the current filling stage, no hydrostatic pressure acts on any of the silo elements. The parts of silo elements loaded in the current filling stage are subjected to pressures from the effective stresses that resulted from dissipation of the pore-water pressures during that stage, whereas the other parts that were loaded in the preceding filling stages are subjected to pressures from the effective stresses that resulted from the current filling stage, in addition to the existing pressures from the effective stresses that resulted from the preceding filling stages.

The pressure distributions along both the silo wall and the hopper due to filling scheme 4 under the drained condition are plotted in Figs. 6a and 6b, respectively. Also plotted in Fig. 6a are the pressure distributions calculated from Janssen's theory using the K values 0.333 and 0.500 computed from eqs. [2] and [3], respectively, and $\mu_s = \tan(0.7\varphi) = 0.384$. These two pressure distributions are denoted in Fig. 6a by Janssen (1) and Janssen (2), respectively. The maximum values for the wall pressures from the three filling stages are about 16, 30, and 46 kN/m^2, respectively. The corresponding maximum values for the fourth filling stage from Janssen's theory are approximately 41 and 55 kN/m^2, respectively, for the two K values 0.333 and 0.500. It can be seen from Fig. 6a that the pressure distribution predicted for the fourth filling stage agrees very well with Janssen's pressure distribution calculated using the coefficient of active earth pressure; however, Janssen's theory underestimates the maximum pressure value at the wall bottom by about 9%. It is clear that the finite-element predictions obtained here using the example silo are much closer to Janssen's predictions than those obtained in the comparative study shown earlier in this investigation. The difference between the two cases concerns the geometric properties of the structure and the boundary conditions at the level of the wall base. In addition to the different slenderness and aspect ratios adopted for the two structures, the bulk solids in the first case (comparative study) were assumed to be restrained in the vertical direction at the base,

Fig. 4. Results obtained from the closed-form and finite element (FE) solutions: (*a*) wall pressure distribution, and (*b*) axial and hoop force distributions.
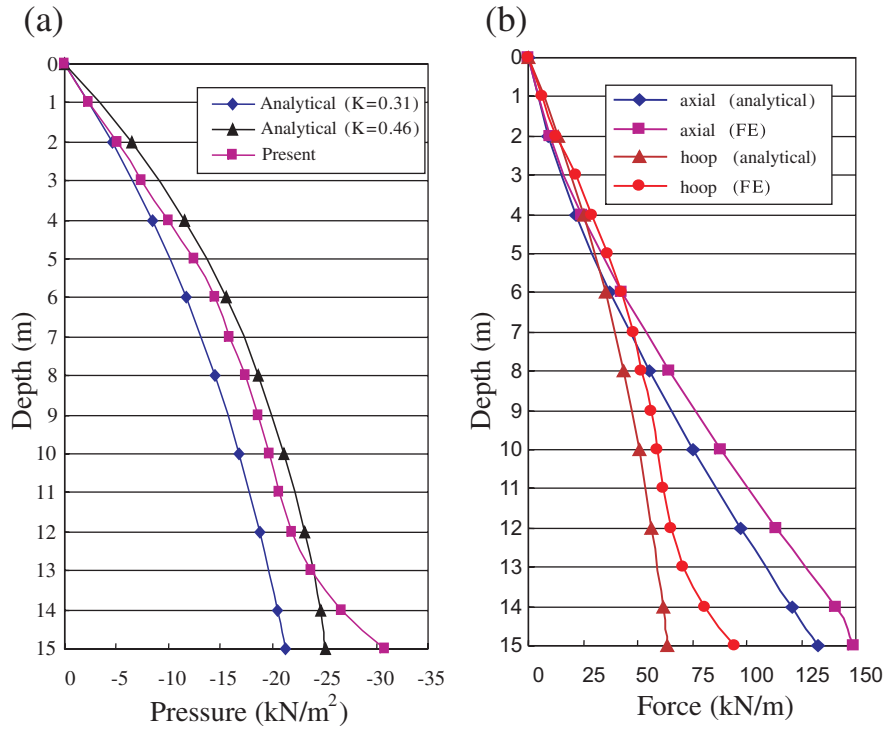
**Fig. 5.** Variation of excess pore-water pressure in bulk solids.
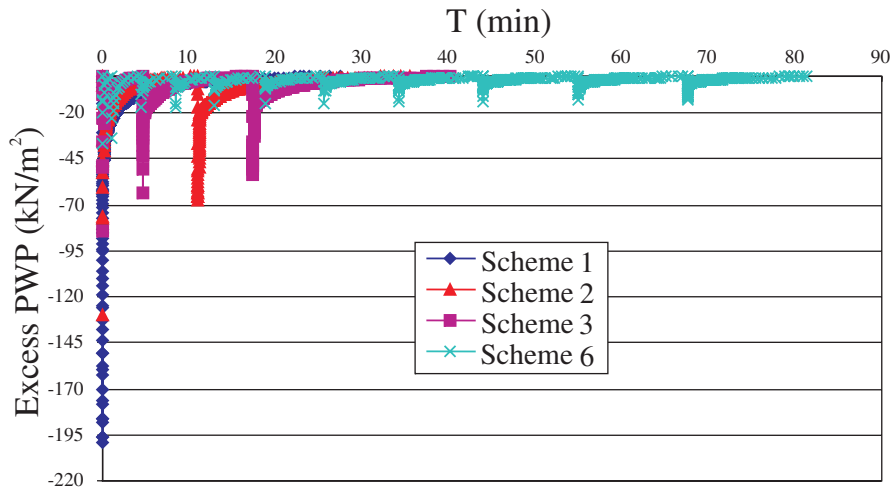
whereas those in the second case are supported by the bulk solids in the hopper. Moreover, the wall bottom tip is free to move laterally in the first case, but its lateral movement is partially restrained in the second case. It is apparent that further investigations are still needed into both the proper finite-element modeling of silo loading problems and the range of applicability of the silo classic theories. This is not treated here, however, since it is beyond the scope of the current investigation.

Under the undrained condition, the maximum values for the hydrostatic pressures on the wall from the three filling stages are about 48, 54, and 60 kN/m^2, respectively. These maximum values occur at the bottom of the wall.

Figure 6*b* shows that, except for the pressure distribution due to filling stage 1 (hopper filling) where the maximum pressure occurs at the bottom of the hopper (zero *x* coordinate), the maximum pressures due to the subsequent filling stages occur in the vicinity of the hopper mid-span. The maximum values for the hopper pressures from the four filling stages 1–4 are about 37, 65, 88, and 100 kN/m^2, respectively. The increase in the pressure due to a subsequent filling stage is higher at the top of the hopper. For instance, the increases in the pressures due to filling stage 2 are about 17 and 36 kN/m^2 at the bottom and top of the hopper, respectively.

Under the undrained condition, the maximum values for the hydrostatic pressures on the hopper from the four filling

Fig. 6. Pressure distributions on silo elements due to filling scheme 4: (*a*) wall, and (*b*) hopper.
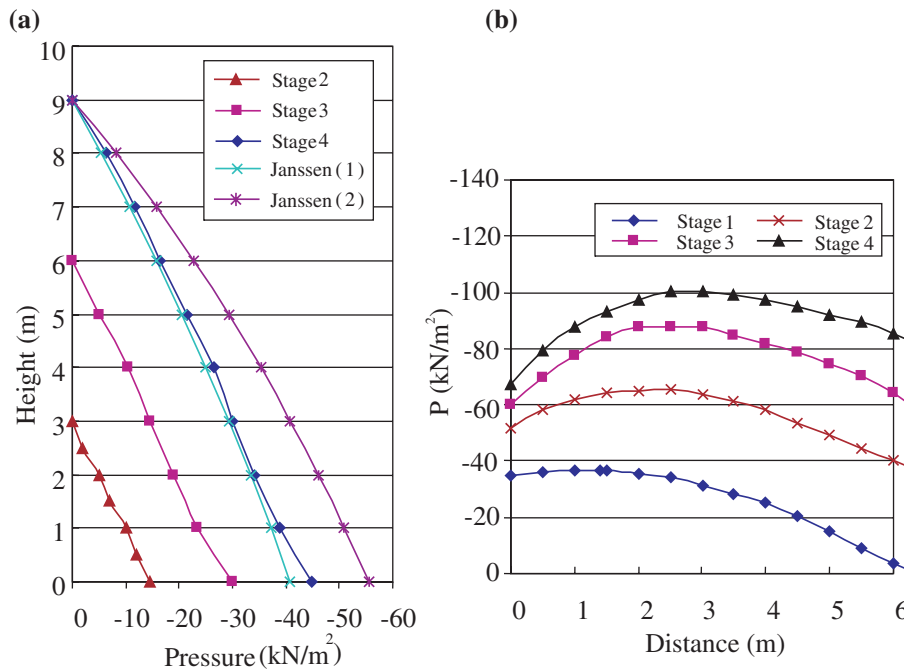
stages are about 69 kN/m^2 from the first filling stage and 50 kN/m^2 from the subsequent stages.

Distribution of internal forces

Since this investigation focuses primarily on the effects of silage consolidation on the internal forces that develop in the silo elements due to filling, it is appropriate first to illustrate the typical patterns of these forces. Figure 7 shows the distributions of the axial, hoop, and shear forces and the meridianal bending moments for filling scheme 2 due to the drained condition. For the membrane forces, the positive sign denotes tension and the negative sign denotes compression. The bending moments are considered positive when they produce tension in the outside fiber of the silo element. The following observations can be made from Fig. 7. The silo elements in the vicinity of the wall–hopper junction are subjected to hoop compression (Fig. 7*b*), and the maximum bending moments and shears in all elements occur at the wall–hopper junction (Figs. 7*c*, 7*d*).

The variation of the wall thickness along the lower 3.0 m has been modeled using three beam elements of average thicknesses 0.275, 0.225, and 0.175 m, and this explains the sharp changes in the hoop force distribution along the silo wall plotted in Fig. 7*b*.

Maximum axial loads

The maximum axial loads in both the silo wall and hopper are plotted in Fig. 8. The maximum axial load in the wall is higher for the drained condition. For filling scheme 1, for instance, the axial load due to the drained condition is about 85% higher than that due to the undrained condition. This percentage decreases as the number of filling stages increases until it reaches about 10% for scheme 6. This is due to the increase in the relative vertical movement between the ensiled material and the wall at the interface, resulting from the settlement of the ensiled material due to consolidation. It

can also be seen that the maximum axial load associated with the undrained condition is higher for filling schemes with a greater number of filling stages. For example, the axial load due to filling scheme 6 (11 layers) is approximately 60% higher than that predicted due to filling scheme 1 (one layer). This is because the excess pore-water pressure developed in each specific layer is permitted to fully dissipate prior to adding the next layer. Thus, the one-step filling scheme (scheme 1) is characterized by the development of maximum pore-water pressure, and accordingly the least maximum axial load in the wall.

For the maximum axial loads in the hopper, a trend opposite to that of their counterparts in the wall can be observed in Fig. 8. This may be attributed to the fact that the drained condition is associated with an increase in the portion of load transferred to the wall, and consequently a decrease in that acting on the hopper.
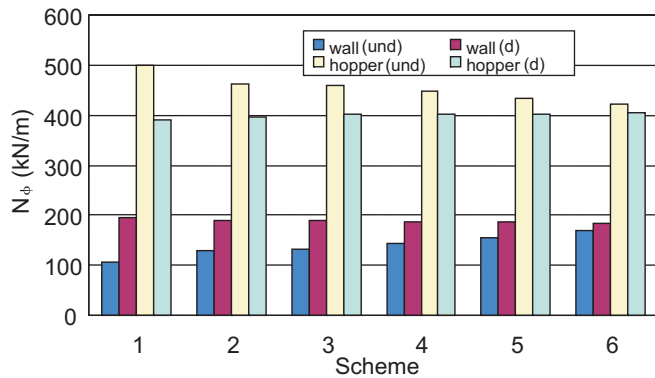
Maximum hoop forces

The maximum hoop tensions and compressions in the wall due to the six filling schemes are presented in Fig. 9. The maximum tension is associated with the undrained condition, whereas the maximum compression is associated with the drained condition. This is because the increase in the excess pore pressure within the bulk solids (the undrained condition) causes an increase in the wall outward movements but a decrease in its inward movements; the latter occurs at the wall–hopper junction.

For filling scheme 1 (one layer) the maximum tension due to the undrained condition is about 170% higher than that due to the drained condition. This percentage decreases as the number of filling stages increases until it reaches about 20% for filling scheme 6. The undrained prediction of scheme 6 is approximately 58% less than its counterpart due to scheme 1. This is because filling scheme 6 is characterized by full dissipation of the excess pore pressure following

Fig. 7. Distribution of internal forces in silo elements: (*a*) axial force, (*b*) hoop force, (*c*) shear force, and (*d*) bending moment. The positive signs denote tension, and the negative signs compression.
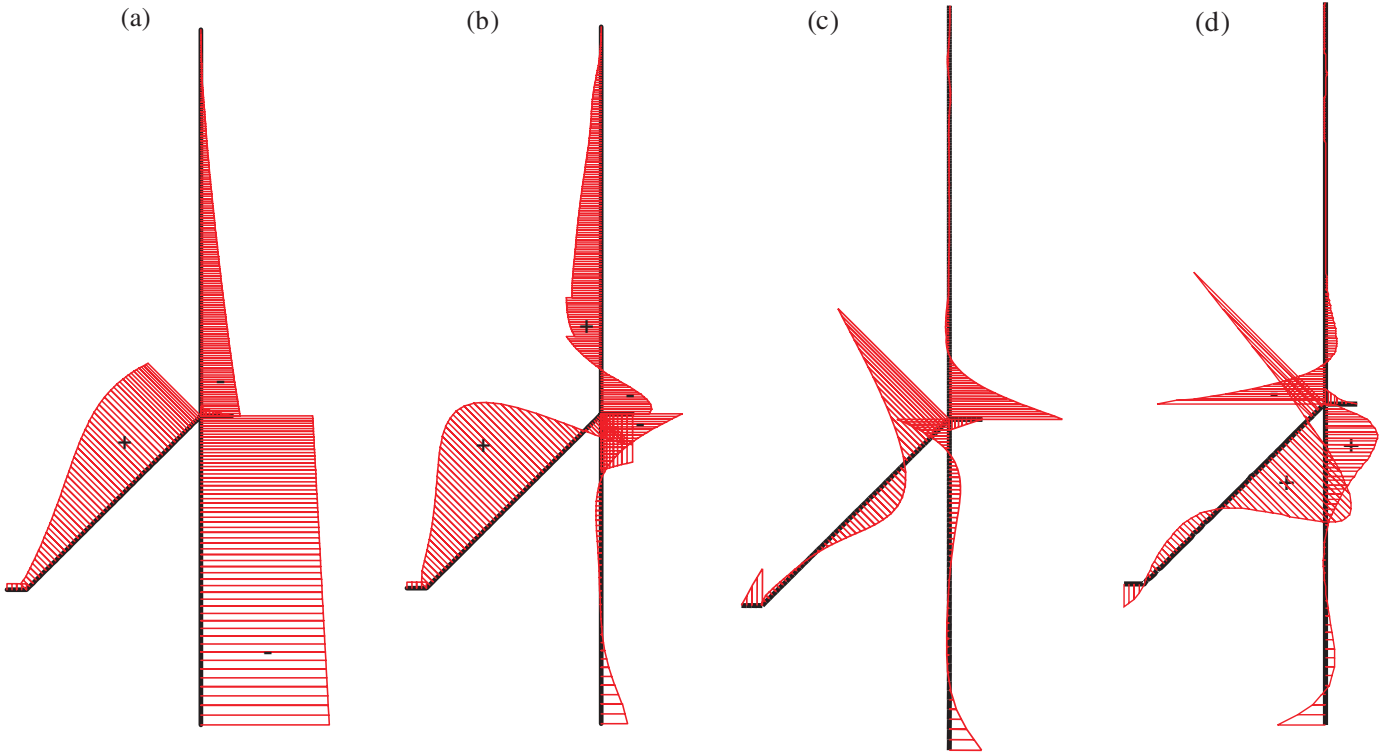
Fig. 8. Maximum axial forces due to different filling schemes in the wall and hopper. d, drained; und, undrained.


Fig. 9. Maximum tensile (tens) and compressive (comp) hoop forces in the wall. d, drained; und, undrained.
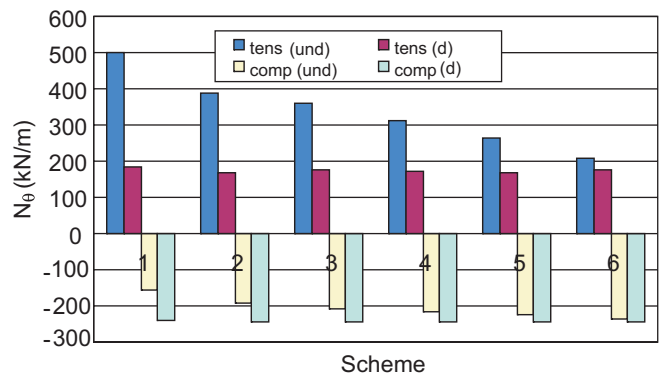
completion of each filling stage. It can also be seen that for filling scheme 1 the maximum compression due to the drained condition is about 58% higher than that due to the undrained condition. The absolute maximum value of the hoop force is due to tension for schemes 1–5 but compression for scheme 6 only. This implies that filling schemes with a number of layers higher than scheme 6 will be characterized by absolute maximum values due to compression.

The maximum hoop tensions and compressions in the hopper due to the six filling schemes are presented in Fig. 10, which shows a trend similar to those in the wall. For filling scheme 1, the maximum tension due to the undrained condition is about 51% higher than that due to the drained condition. This percentage decreases as the number of filling layers increases until it reaches about 6% for scheme 6. The

Fig. 10. Maximum tensile (tens) and compressive (comp) hoop forces in the hopper. d, drained; und, undrained.
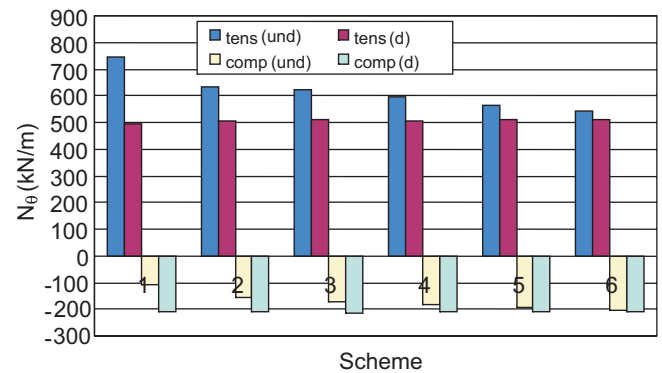
undrained prediction of scheme 6 is approximately 38% less than its counterpart due to scheme 1. For filling scheme 1, the maximum compression due to the drained condition is about 96% higher than that due to the undrained condition. Thus, for the rapid filling process (scheme 1) the maximum hoop tension in the wall is more sensitive to the bulk solids condition than that in the hopper, as can be inferred from the comparison between Figs. 9 and 10. By contrast, the maximum hoop compression in the hopper is more sensitive to the condition of the bulk solids than is the hoop compression in the wall.

The maximum hoop compressions in both the ring beam and supporting wall are plotted in Fig. 11. Again, as with those in the wall and hopper, the maximum compressions occur due to the drained condition. For filling scheme 1, the maximum compression in the ring beam due to the drained condition is about 44% higher than that due to the undrained condition. This percentage drops to only 2% for scheme 6, in which more periods of full drainage are permitted. Similar observations can be made for the maximum compressions in the supporting wall.

Maximum shear forces

The maximum shear forces in both the wall and hopper due to the six filling schemes are given in Fig. 12. The general trend in Fig. 12 is that the undrained predictions are higher, and this is more pronounced for schemes with a lower number of filling stages. For instance, the undrained maximum shears in the wall due to schemes 1 and 6 are, respectively, 63% and 9% higher than the drained maximum shears, but in the hopper the corresponding percentages are 33% and 6% higher. In other words, the shear forces in the hopper are less sensitive to the drainage condition of the bulk solid than are the shear forces in the wall.
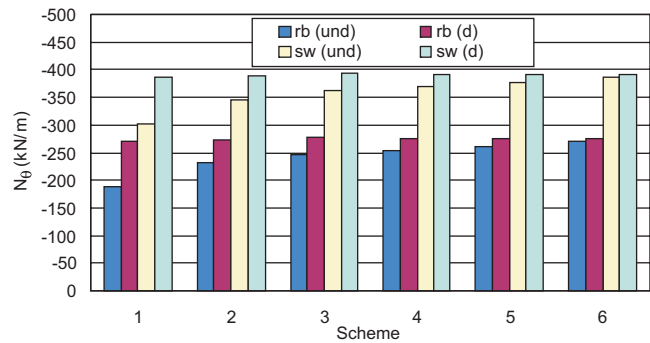
Maximum bending moments

The maximum bending moments in both the wall and hopper due to the six filling schemes are presented in Fig. 13. For the negative bending moments, the undrained predictions are higher than the drained predictions, and this is more distinguished for filling schemes with a lower number of stages. For both the wall and hopper, the undrained predictions due to schemes 1 and 6 are, respectively, 45% and 7% higher than the drained predictions. For the maximum positive bending moments in the hopper, a trend similar to that of the negative bending moments can be observed. Nevertheless, these predictions are less sensitive to the bulk solid condition (undrained or drained) than those of the negative bending moments, as the undrained predictions due to schemes 1 and 6 are, respectively, 16% and 4% higher than the drained predictions.

Effect of ring beam stiffness

To examine the effect of the ring beam stiffness on the internal forces in the silo elements, the example silo was first analyzed without a ring beam for the two limiting cases of zero lateral restraint (case 1) and infinitely stiff lateral restraint (case 2) at the wall–hopper junction. The analyses were conducted for filling scheme 3 under the drained condition. The results obtained have shown that the hoop forces
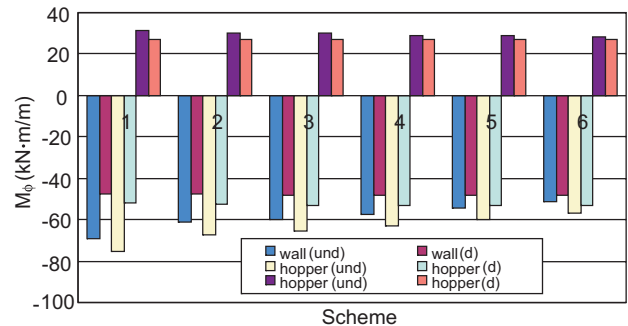
Fig. 11. Maximum hoop forces in the ring beam (rb) and supporting wall (sw). d, drained; und, undrained.

Fig. 12. Maximum shear forces in the wall and hopper. d, drained; und, undrained.
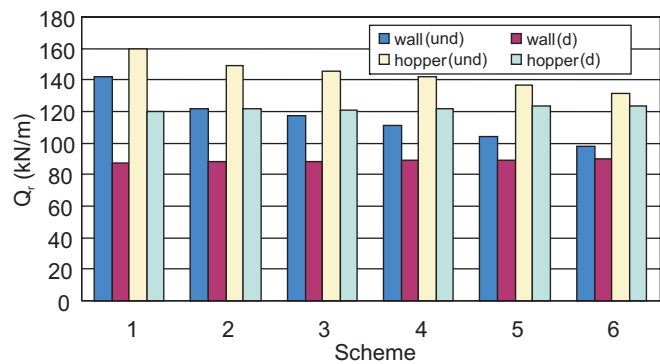
Fig. 13. Maximum bending moments in the wall and hopper. d, drained; und, undrained.

Table 1. Hoop forces (N_θ) in silo elements at the wall–hopper junction due to two limiting cases of lateral support stiffness.

Case	N_θ (kN/m)		
	Hopper	Silo wall	Supporting wall
1	−304	−292	−480
2	80	−39	−106

in the silo elements are the most influenced by the restraint stiffness at the wall–hopper junction. For other internal forces, the maximum difference between the results obtained is within the range of 2%–10%, and accordingly they are not shown here. The magnitudes of the hoop forces in the silo

Table 2. Hoop forces (N_θ) in silo elements at the wall–hopper junction due to four ring beam configurations.

Dimensions		N_θ (kN/m)			
Breadth (m)	Thickness (m)	Ring beam	Hopper	Silo wall	Supporting wall
0.40	0.40	–316	–250	–256	–428
0.40	0.60	–294	–229	–243	–408
0.40	0.80	–274	–211	–230	–391
0.40	1.20	–242	–181	–210	–362

elements at the wall–hopper junction for cases 1 and 2 are listed in Table 1. As shown in Table 1, an infinitely stiff lateral restraint (case 2) at the wall–hopper junction causes significant drops in the magnitudes of the hoop compressions in both the silo wall and the supporting wall and a change in the type of hoop force in the hopper from compressive to tensile. The magnitudes of the hoop compressions in the silo wall and supporting wall are 292 and 480 kN/m, respectively, for case 1 compared with 39 and 106 kN/m for case 2. The magnitudes of the hoop forces in the hopper are 304 kN/m (compression) and 80 kN/m (tension) for cases 1 and 2, respectively.

It is therefore evident that the magnitude and possibly the type (tensile or compressive) of the hoop force in the silo elements at the wall–hopper junction are dependent on the magnitude of the lateral displacement allowed at this location. This displacement magnitude may be controlled by the designer through the dimensions chosen for the silo elements at the wall–hopper junction. To confirm this, the example silo was further analyzed for ring beam thicknesses of 0.40, 0.60, 0.80, and 1.20 m measured from the supporting wall centreline, with a constant breadth of 0.40 m, and the magnitudes of the lateral displacements obtained at the wall–hopper junction are 0.160, 0.150, 0.141, and 0.126 mm for the four ring beam configurations considered, respectively. The magnitudes of the hoop forces in the silo elements at the wall–hopper junction are listed in Table 2 for the four ring beam configurations. Again, as the lateral displacement at the wall–hopper junction decreases, or in other words as the ring beam stiffness increases, the magnitude of the hoop compression decreases. As the beam thickness is increased from 0.40 to 1.20 m, the magnitudes of the hoop compressions in the ring beam, hopper, silo wall, and supporting wall drop by about 24%, 28%, 18%, and 15%, respectively.

Effect of boundary conditions

The foregoing results were obtained for lateral restraint applied to the wall top. A silo free at its top is considered here to examine the effect of that restraint. The results obtained for scheme 3 (drained condition) due to these two different boundary conditions are listed in Table 3. It is clear from Table 3 that the lateral restraint at the wall top has a negligible effect on the results obtained.

Conclusions

A finite-element solution is presented for the internal forces in an example elevated concrete silo due to filling. The results are obtained using an axisymmetric finite-element model rep-

Table 3. Internal forces due to two different boundary conditions.

Internal force	Laterally restrained top		Free top	
	Wall	Hopper	Wall	Hopper
N_ϕ (kN/m)	–188.95	401.00	–189.65	399.70
N_θ (kN/m)	176.30	509.00	176.33	504.08
	–245.40	–213.90	–242.93	–210.74
Q_r (kN/m)	88.60	121.25	88.83	121.00
M_ϕ (kN·m/m)	48.22	52.90	48.07	52.55

resenting the silo structure and stored material. The silo is filled with a saturated granular material according to a multistage filling process. The results of analyses are obtained due to both undrained and drained conditions.

A number of conclusions can be drawn for the combination of materials, geometry, and loading considered in this investigation.

Except for the membrane (axial and hoop) compressions that are maximized due to full drainage of the solids, the development of excess pore pressure during the filling process may temporarily cause significant increases in the magnitudes of other internal forces in the silo elements. The proportions of these increases are dependent on the type of internal force and the silo element in which it develops. The most pronounced increase is that in the hoop tension in the wall, predicted here as 170% for the rapid filling scheme (scheme 1). On the other hand, the least pronounced increase is that in the positive bending moment in the hopper, predicted here as 16% for that scheme. Thus, care should be taken when dimensioning a particular silo element for a specific type of internal forces, since the design values at different locations may correspond to different bulk solid conditions (undrained or drained). For example, while dimensioning the silo wall or hopper for hoop forces, the maximum tension would correspond to the undrained condition, whereas the maximum compression would correspond to the drained condition.

Thus, achieving an economic silo design makes the filling rate a factor that should be considered. This time-dependent effect of the filling process can be minimized if reasonable, practical time intervals are left between the filling stages, so the accumulated pore pressures are allowed to dissipate prior to commencement of the next filling stage. Indeed, filling with materials having lower permeability will require a longer time interval for dissipation of the pore pressure. Naturally, that time interval should be acceptable from a practical standpoint, considering the operations of the bulk solids han-

dling facility. Otherwise, the facility use should include delays to permit dissipation of the pore pressures.

From a practical viewpoint, the ring beam stiffness may have an effect on the hoop compressions in the silo elements, but not on other types of internal forces.

The lateral restraint at the top of the wall has a negligible effect on the forces that develop in the silo elements.

The results obtained from this investigation may be useful when planning a field-testing program and may assist during evaluation of existing concrete silos. Following experimental evaluation, the proposed analysis methodology might be used in concrete silo design.

Acknowledgements

References

Abdel-Fattah, M.T., Moore, I.D., and Abdel-Fattah, T.T. 2005. A numerical investigation into the behavior of ground-supported concrete silos filled with saturated solids. International Journal of Solids and Structures. In press. doi:10.1016/j.ijsolstr.2005.06.004 [available online 2 August 2005].

Abdel-Sayed, G., Monasa, F., and Siddall, W. 1985. Cold-formed steel farm structures, Part I: grain bins. ASCE Journal of Structural Engineering, **111**(10): 2065–2089.

ACI. 1997. Standard practice for design and construction of concrete silos and stacking tubes for storing granular materials (ACI 313-97). American Concrete Institute (ACI), Detroit, Mich.

Bishara, A.G., Mahmoud, M.H., and Chandrangsu, K. 1977. Finite-element formulation for farm silo analysis. ASCE Journal of the Structural Division, **103**(ST10): 1903–1919.

Bishara, A.G., Ayoub, S.F., and Mahdy, A.S. 1983. Static pressures in concrete cylinders storing granular materials. Journal of the American Concrete Institute, **80**(3): 210–216.

Briassoulis, D. 1991. Limitations in the range of applicability of the classic silo theories. ACI Structural Journal, **88**(4): 437–444.

Briassoulis, D. 1998. Finite-element analysis of a cylindrical silo shell under unsymmetrical pressure distributions. *In* Advances in civil and structural engineering computing for practice. *Edited by* B.H.V. Topping. Civil-Comp Press, Edinburgh, UK. pp. 31–39.

Brinkgreve, R.B.J., and Vermeer, P.A. 1998. PLAXIS version 7: finite-element code for soil and rock analyses. A.A. Balkema, Rotterdam, The Netherlands.

Cowin, S.C. 1979. Pressure ratio in the theory of bin-pressures. Journal of Applied Mechanics, **46**: 524–528.

Dabrowski, R. 1985. Discussion of "Design pressures in circular bins." ASCE Journal of Structural Engineering, **111**(9): 2074–2076.

DIN. 1987. Design loads for buildings: loads in silo containers, Part 6 (DIN 1055). Deutsches Institut für Normung (DIN), Berlin, Germany.

ECS. 2004. Eurocode 1: basis of design and actions on structures. Part 4: silos and tanks. EN 1991-4, European Committee for Standardization (ECS), CEN, Brussels, Belgium.

Gaylord, E.H., and Gaylord, C.N. 1984. Design of steel bins for storage of bulk solids. Prentice-Hall Inc., Englewood Cliffs, N.J.

Gurfinkel, G. 1979. Reinforced-concrete bunkers and silos. *In* Structural engineering handbook. 2nd ed. *Edited by* E.H.

Gaylord, Jr., and C.N. Gaylord. McGraw Hill, New York, N.Y. p. 22.

Hatfield, F.J., and Bartali, E. 1988. Static forces and moments in a grain silo. ASCE Journal of Structural Engineering, **114**(12): 2814–2819.

Holst, J.M.F.G., Ooi, J.Y., Rotter, J.M., and Rong, G.H. 1999. Numerical modelling of silo filling. I: continuum analysis. ASCE Journal of Engineering Mechanics, **125**(1): 94–103.

Janbu, J. 1963. Soil compressibility as determined by oedometer and triaxial tests. *In* Proceedings of the European Conference on Soil Mechanics and Foundation Engineering, Wiesbaden, Germany. Vol. 1. pp. 19–25.

Janssen, H.A. 1895. Versuche uber Getreidedruck in Silozellen. Zeitschrift des Vereines Deutscher Ingenieure, Duesseldorf, Germany.

Jenike, A.W., Johanson, J.R., and Carson, J.W. 1973. Bin loads — part 2: Concepts; part 3: Mass flow bins. Journal of Engineering for Industry, Transactions of the ASME, Series B, **95**(1): 1–12.

NRCC. 1995. National Farm Building Code of Canada. Canadian Commission on Building and Fire Codes, National Research Council of Canada, Ottawa, Ont.

Ooi, J.Y., and Rotter, J.M. 1990. Wall pressures in squat steel silos from simple finite element analysis. Computers and Structures, **37**(4): 361–374.

Ooi, J.Y., Pham, L., and Rotter, J.M. 1990. Systematic and random features of measured pressures on full-scale silo walls. Journal of Engineering Structures, **12**(2): 74–87.

Pieper, K., and Wenzel, F. 1964. Pressure conditions in silos. W. Ernst and John, Berlin, Germany.

Reimbert, M.L., and Reimbert, A.M. 1976. SILOS — theory and practice. 1st ed. Trans-Tech Publications, Clausthal-Zellerfeld, Germany.

Rotter, J.M. 1990. Structural design of light-gauge silo hoppers. ASCE Journal of Structural Engineering, **116**(7): 1907–1922.

Schanz, T. 1998. Zur Modellierung des Mechanischen verhaltens von Reibungsmaterialen, Habilitation. Stuttgart Universität, Stuttgart, Germany.

Walker, D.M. 1966. An approximate theory for pressure and arching in hoppers. Chemical Engineering Science, **21**: 975–997.

Walters, J.K. 1973. A theoretical analysis of stresses in axially-symmetric hoppers and bunkers. Chemical Engineering Science, **28**(3): 779–789.

List of symbols

c cohesion

c^{ref} coefficient of isotropic permeability

E Young's modulus

E_{oed} oedometer stiffness

$E_{\mathrm{oed}}^{\mathrm{ref}}$ tangent stiffness

E_{ur} stress-dependent stiffness modulus

$E_{\mathrm{ur}}^{\mathrm{ref}}$ reference stiffness modulus for unloading and reloading

E_{50} confining-stress-dependent stiffness modulus for primary loading

E_{50}^{ref} reference stiffness modulus corresponding to the reference confining pressure

f yield function

$\bar{f}$ stress function

G shear modulus

K pressure ratio

m power of stress dependency of bulk solid material stiffness

M bending moment
N membrane force
P pressure
P^{ref} reference confining pressure
q deviatoric stress
q_a asymptotic deviatoric stress
q_f ultimate deviatoric stress
Q shear force
Q_r radial shear force
r silo radius
R strength factor
R_f failure ratio
T time
y depth measured from top of silage
ε strain
ε_1 vertical strain
$\varepsilon_1^e, \varepsilon_2^e, \varepsilon_3^e$ elastic strains
ε_1^p axial plastic strain
ε_v^p volumetric plastic strain
γ unit weight
γ_d dry unit weight
γ_{wt} wet unit weight

γ^p function of plastic strains
μ coefficient of friction
ν Poisson's ratio
ν_{ur} unloading–reloading Poisson's ratio
σ normal stress
σ_1' vertical stress
σ_3' confining pressure
φ angle of internal friction
φ_{cv} critical state friction angle
φ_m mobilized friction angle
ψ angle of dilatancy
ψ_m mobilized angle of dilatancy

Subscripts

int interface
s stored material
ϕ meridianal direction
θ circumferential direction